The link between gliomas infiltration and white matter architecture investigated with electron microscopy and diffusion tensor imaging

Francesco Latini [a,*], Markus Fahlström [b], Andrea Beháňová [c], Ida-Maria Sintorn [c], Monika Hodik [d], Karin Staxäng [d], Mats Ryttlefors [a]

[a] *Department of Neuroscience, Neurosurgery, Uppsala University, Uppsala, Sweden*
[b] *Department of Surgical Sciences, Radiology, Uppsala University, Uppsala, Sweden*
[c] *Department of Information Technology, Uppsala University, Uppsala, Sweden*
[d] *Immunology, Genetics and Pathology - Biovis Platform, Uppsala University, Uppsala, Sweden*

ARTICLE INFO

ABSTRACT

Diffuse low-grade gliomas (DLGG) display different preferential locations in eloquent and secondary associative brain areas. The reason for this tendency is still unknown. We hypothesized that the intrinsic architecture and water diffusion properties of the white matter bundles in these regions may facilitate gliomas infiltration. Magnetic resonance imaging of sixty-seven diffuse low-grade gliomas patients were normalized to/and segmented in MNI space to create three probabilistic infiltration weighted gradient maps according to the molecular status of each tumor group (IDH mutated, IDH wild-type and IDH mutated/1p19q co-deleted). Diffusion tensor imaging (DTI)- based parameters were derived for five major white matter bundles, displaying regional differences in the grade of infiltration, averaged over 20 healthy individuals acquired from the Human connectome project (HCP) database. Transmission electron microscopy (TEM) was used to analyze fiber density, fiber diameter and g-ratio in 100 human white matter regions, sampled from cadaver specimens, reflecting areas with different gliomas infiltration in each white matter bundle. Histological results and DTI-based parameters were compared in anatomical regions of high- and low grade of infiltration (HIF and LIF) respectively. We detected differences in the white matter infiltration of five major white matter bundles in three groups. Astrocytomas IDHm infiltrated left fronto-temporal subcortical areas. Astrocytomas IDHwt were detected in the posterior-temporal and temporo-parietal regions bilaterally. Oligodendrogliomas IDHm/1p19q infiltrated anterior subcortical regions of the frontal lobes bilaterally. Regional differences within the same white matter bundles were detected by both TEM- and DTI analysis linked to different topographical variables. Our multimodal analysis showed that HIF regions, common to all the groups, displayed a smaller fiber diameter, lower FA and higher RD compared with LIF regions. Our results suggest that the both morphological features and diffusion parameters of the white matter may be different in regions linked to the preferential location of DLGG.

1. Background

Diffuse low-grade gliomas (DLGG) are WHO grade-II tumors, originating from glia cells and characterized by relatively slow growth but extensive cerebral infiltration. Their kinetic features reflect the complex dynamic interaction over time with the surrounding brain (Alfonso et al., 2017; Kansal et al., 2000). Differences in cortical subcortical infiltration and dislocation patterns are related to the histological origin (astrocytes, or oligodendrocytes) and may depend on their localization and the consequent permissive nature of neighboring structures around the tumor. In fact, gliomas dissemination occurs much faster along the white matter bundles than trough cortical areas (Smits et al., 2015; Szalisznyo et al., 2013). Glioma cells actively migrate through the tortuous extracellular spaces of the brain, which leads to the formation of distant satellite tumors. Hence, they behave much like non-malignant brain cells during embryonic development, or adult stem cells in the mature brain, which similarly migrate along extracellular routes, often exploiting nerve bundles as guides (Cuddapah et al., 2014).

Some studies even suggest that a difference in the direction of the white matter bundles (parallel or perpendicular to the tumor front cells)

may influence the gliomas infiltration in different ways and velocities (Painter and Hillen, 2013). The initial tumor location and the architecture of the peritumoral tissue are therefore very important for the comprehension and prediction of the possible infiltration patterns. Different preferential locations among DLGG subtypes have also been described with possible link to gliogenesis or cell migration during the developmental stages (Latini et al., 2020a; Skjulsvik et al., 2020). A common preferential location for DLGG within the so called "minimal common brain" has been suggested (Ius et al., 2011; Parisot et al., 2016; Sarubbo et al., 2015) with consequent infiltration of crucial white matter bundles (Duffau and Capelle, 2004; Latini et al., 2020a, 2019; Mandonnet et al., 2006).

These specific tumor features impose a major challenge on the clinical management, requiring an individualized approach for each patient to decide optimal treatment strategies (Smits and Jakola, 2019). The extent of surgical resection is established to be an important element affecting the overall survival in these patients (Jakola et al., 2014, 2012, 2013). However, the extent of resection is often limited by eloquent structures and non-compensable networks inside or in close proximity to the tumor radiological border. The possibility to better understand the interplay between gliomas and white matter anatomy is of paramount importance to tailor individual treatments. A possible grade of invasiveness has been identified for different types of DLGG using new classification tolls based on white matter infiltration (Latini et al., 2020a, 2019). These studies suggest that the preferential location of these tumors reflect a higher infiltration of specific white matter bundles at the moment of radiological diagnosis. Among these bundles specific regions in the fronto-temporo-insular areas were more often detected as infiltrated compared with other, more posterior regions (Latini et al., 2020a; Skjulsvik et al., 2020). The reason for this tendency is still unknown. We hypothesize that a possible favorable factor for tumor infiltration, may depend on the intrinsic architectural and diffusion proprieties of the infiltrated white matter bundles such as fiber density, diameter, or myelin thickness.

To test this hypothesis, we analyzed white matter infiltration in a cohort of patients with different molecular subtypes of DLGG using frequency/gradient maps. We used transmission electron microscopy (TEM) to analyze human white matter regions, sampled from cadaver specimens, reflecting different gliomas infiltration frequency. Finally, we compared the histological results with diffusion parameters of the same regions in healthy individuals. We aimed to understand whether specific features of the analyzed white matter pathways may reflect the differences in observed gliomas infiltration.

2. Materials and methods

2.1. Probabilistic map of white matter infiltration

2.1.1. Patient population

We collected radiological data for all patients (>18 years) diagnosed at the Department of Neurosurgery, Uppsala University Hospital between February 2005, and December 2015 with DLGG. Diffuse low-grade astrocytomas (WHO grade II, IDH mutant and IDH wild type) and oligodendrogliomas (WHO grade II, IDH1mutant /1p19q co-deleted) were used for this study as a population with molecular confirmed diagnosis according to the WHO-2016 classification (Louis et al., 2016) from a previously reported cohort (Latini et al., 2020a).

The diagnosis was assessed as previously reported by our group for different studies involving DLGG cohorts before 2016 (Elsir et al., 2011; Popova et al., 2014; Zetterling et al., 2017, 2016). Shortly, all sections were stained with H & E. Mutated isocitrate dehydrogenase 1 (IDH1) R132H protein, was detected using a monoclonal mouse antibody targeting the mutated IDH1 R132H protein (mIDH1R132) as a part of tissue micro-array panel (Capper et al., 2009; Popova et al., 2014; Zetterling et al., 2016). In cases before 2013, detection of losses of chromosomal arms 1p and 19q was performed by fluorescent in situ hybridization

analysis (FISH), as previously described (Elsir et al., 2011). Since 2013 and for all reassessed cases, detection of losses of chromosomal arms 1p and 19q was performed using a multiplex ligation-dependent probe amplification (MLPA) based assay (MRC-Holland), using Coffalayser. Net (2012) (Zetterling et al., 2017). Validation of the MPLA method was performed as previously described (Natté et al., 2005).

The regional ethics committee, Regionala Etikprövningsnämnden Uppsala, approved the study protocol (Dnr 2015/210). Data were collected retrospectively and anonymously; hence no informed consent from patients included in this study was needed.

2.1.2. Radiological data

Morphological magnetic resonance imaging (MRI) sequence; T2-weighted Fluid Attenuated Inversion Recovery (T2-FLAIR) or T2-weighted Turbo Spin Echo (T2-TSE) acquired at the moment of radiological diagnosis of all the patients were normalized to Montreal Neurological Institute (MNI) space using the built-in normalizing software in DSI studio (DSI Studio, http://dsi-studio.labsolver.org). The non-linear registration box included an affine registration part and a diffeomorphic mapping method, defined contour driven match (CDM); standard parameters (resolution 2, smoothness 0.30 and 60 steps) were chosen for the registration process. T2-FLAIR slice thickness ranged between 1 mm and 5 mm and in-plane resolution was 0.5–2 mm. The registration was systematically checked visually in all cases before the next step with adjustment registration box. The corpus callosum and fourth ventricle were used as anatomical landmarks for sagittal slices, lateral ventricles, and the contour of fronto parietal cortices were used as anatomical landmarks on the axial slices and body of corpus callosum and third ventricle were used as references on coronal slices. Manual adjustment was possible but not needed in any case.

The total lesion was successively manually segmented on original morphological MRI by the first author with DSI studio in MNI space. Three different gradient probabilistic infiltration weighted gradient maps were obtained by computing the cumulative number of observed lesions for each voxel and dividing by the total amount of lesions (Ius et al., 2011; Latini et al., 2020a) in three different groups: Astrocytomas IDHm, Astrocytomas IDHwt and Oligodendrogliomas.

Based on previous results we selected five major white matter bundles which showed regional differences of infiltration frequency (Latini et al., 2020a) and were at the same time accessible to a standardized/reproducible white matter dissection technique and anatomically identifiable based on cortical-subcortical topographical anatomy. The genu of corpus callosum (CC), the cingulum (Ci), the arcuate fasciculus (AF), inferior fronto-occipital fasciculus (IFOF) and the cortico-spinal tract (CST) were reconstructed within the HCP 1021 template following the anatomical criteria already published with the Brain Grid DTT reference atlas (Latini et al., 2020a, 2019) and merged with probabilistic infiltration weighted gradient map.

2.2. Transmission electron microscopy (TEM)

2.2.1. Acquisition of cadaver specimens

Ten normal cerebral hemispheres (five right and five left) donated to the Department of Medical Cell Biology, Section for Anatomy Studies at Uppsala University, Sweden, were used in this study. The hemispheres came from six human cadavers (two males and four females) with the mean age of 76 years (age range 49–89, standard deviation, SD 13) and a mean postmortem interval of 1.6 days (SD 0.4).

All individuals donating had given written consent for use of the whole cadaver for biomedical research and education in a testimonial donation letter. The study protocol was filed with the application for ethical vetting of research involving humans to the Regional Ethical Vetting Board in Uppsala, Sweden (Dnr 2014/468).

2.2.2. Perfusion protocol, specimen preparation

Each brain was fixed with an intra-carotidal injection of 12%

formalin within the first 72 h after death as previously described (Latini et al., 2015). The interval from fixation to dissection was between 6 and 12 months. The hemispheres were then separated by a cut through the midsagittal plane and kept in 5% formalin for another 48 h.

2.2.3. Sample collection

We collected 10 white matter regions for each hemisphere based on probabilistic infiltration map. Two samples were collected from each of the selected white matter bundles: the corpus callosum, the cingulum, the arcuate fasciculus, the inferior fronto-occipital fasciculus, and the cortico-spinal tract. The dissections and sample collections were performed under microscopic magnification (up to 10×). All the blocks had a relatively large areal size of up to 0.5 and 0.8 cm^2. The first block of was sampled from the genu of Corpus callosum identified on the sagittal mesial surface of all hemispheres (Ge). Microscopic metal dissectors and micro blades were used for the dissection of white matter to split or partially peel away the brain cortex, preserving the most superficial intra-cortical and subcortical fibers of the lateral and basal brain surfaces. Following the fibers from the corpus callosum to the callosal radiation a second block was collected deep into the frontal white matter in continuity with the callosal radiation (CaR). The cortex of the cingulum in its frontal component at the level of the SMA/Pre-SMA was dissected and the underlying white matter of the cingulum was collected as a third block (Ci$_F$). The temporal-occipital portion of the cingulum was then identified on the mesial brain surface and the cortex was peeled away to reveal the white matter which was sampled as fourth block (Ci$_T$). The last block was sampled from the anterior cerebral peduncle of the mesencephalon were all the CST fibers converged escaping from the internal capsule region (CST$_{BS}$). The methods and the anatomical landmarks used for the sample collection from the medial surface are displayed in Fig. 1A.

On the lateral surface of the brain the sylvian fissure was opened at the posterior insular point. The deep cortex of the supramarginal gyrus/temporo-parietal operculum was removed under magnification. The first white matter bundles identified at this level was the vertical segment of the superior longitudinal component posteriorly (Latini et al., 2017, 2020b, 2015). The vertical fibers of the arcuate fasciculus were identified medially in respect with vSLF and sampled as AF$_{TP}$. The ventral premotor cortex was then dissected revealing the intermediate subcortical white matter fibers and then the AF fibers were identified as a compact bundle of white matter running medial compared with indirect anterior component of the superior longitudinal fasciculus (hSLF), lateral compared with corona radiata fibers which run perpendicular to the AF fibers. The AF was then sampled in this region as AF$_F$.

Deep in the sylvian fissure, at the intersection between AF fibers and longitudinal fibers from the middle longitudinal fasciculus, the anterior portion of the sagittal stratum of Sachs was identified. A deeper layer with respect to the MdLF was sampled afferent to the inferior fronto-occipital fasciculus (IFOF$_{SSS}$). A dissection at the level of the limen insula was then performed to reveal first the uncinate fasciculus and then the IFOF fibers running through the external capsule region in its anterior part. The IFOF was then sampled as IFOF$_F$.

The central sulcus was identified and dissected from its dorso-lateral surface (hand area). Deeper white matter was identified in respect to the U-fibers between motor and sensory cortices. Vertical fibers originating from the hand area and directed to the corona radiata-capsular region were sampled as cortico-spinal tract (CST$_F$). The anatomical locations and illustrative images of the methods used for the sample collections on the lateral surface of the brain are presented in Fig. 1B.

2.3. Sample preparation and imaging.

A part of the tissue was cut off and used for embedding for TEM. Samples were rinsed in 0.1 M maleate buffer for 10 min prior to 1 h incubation in reduced osmium tetroxide in 0.1 M maleate buffer. After a further rise in 0.1 M maleate buffer, samples were dehydrated in graded alcohols (70%–99.9%) for in total 1 h, followed by 5 min incubation in propylene oxide. The tissue samples were then placed in a mixture of Epon resin and propylene oxide (1:1) for 1 h, followed by two changes of 100% resin, the first for 2–4 h and the last o/n. Subsequently, samples were embedded in capsules in newly prepared Epon resin and left for 1 h and then polymerized at 60 degreesC for 48 h.

The specimens were cut into semi thin sections (1–2 μm), stained in Toluidine Blue and examined in LM to control the presence of cross sectioned axons. The block was trimmed, ultrathin sections (60–70 nm) were cut in a Leica UCT ultramicrotome and placed on a grid. The grids were contrasted in 5% Uranylacetate and 3% Reynolds lead citrate for 10 and 2 min. Grids were examined by TEM (FEI Tecnai G2) operated at 80 kV. The total area explored for each sample was 15 mm^2. For each sample 10–12 images were taken from two areas with the best preserved morphology at 4200× magnification.

2.3.1. Measurement of histological characteristics

High resolution pictures from electron microscopy preparation were uploaded in Parameters Measurement (PM), a dedicated inhouse developed software based on Matlab® (version R2020a, The MathWorks, Inc., Natick, Massachusetts, USA). PM is a software for the interactive measurements of myelinated axons in white matter. The main view of the graphical user interface and the detailed instructions are provided in ESM1.

A scale of 5 μm were utilized in all the pictures as reference for measurement. The area analyzed for each specimen was formed by the two best images (each with an area of 186 μm^2) with a total area for each specimen of 372 μm^2. A sampling area was discarded and replaced by another only if, at high magnification, it turned out that a glia cell body or a blood vessel was captured (because it would fill a large part of the sampling area).

The fibers diameter was measured starting with the inner diameter, defined as the straight line starting from inner borders from the myelin sheath (thus excluding the myelin sheath itself). Then the outer diameter was measured. Since profiles are often not circular but elliptic or elongated, depending on the angle with the plane of section, the largest diameter perpendicularly to the long axis of the profile was measured, parallel to the inner diameter (Liewald et al., 2014; Partadiredja et al., 2003). The g-ratio, defined as the ratio between the inner and the outer diameter of the myelin sheath (Stikov et al., 2015) was automatically calculated by the software. Profiles of myelinated axons extending over the picture borders where discarded, as well as those with an awkward/irregular shape in which a diameter could not be defined, as well as profiles which ran in parallel to the section. Profiles which could not be identified with high probability as axons/fibers were also discarded. In the few remaining questionable cases, the following additional criteria were applied: profiles with only a very thin dark membrane and no internal structure were excluded, as well as profiles in which the membrane could not be clearly delimited from internal structures. An illustration of the measurement procedure is presented in Fig. 2.

2.4. Tractography and virtual dissection of the white matter bundles

2.4.1. Participants

Twenty subjects (12 females and 8 males; age groups 31–35 and 36+) were acquired from the Human Connectome Project (HCP) database as presented in ESM2. The subjects were selected because of the older age group closer to the age of DLGG patients, high quality structural images including T1 and T2 sequence and high angular resolution diffusion imaging (dMRI). The 1200 Subjects Data Release Reference Manual provides full technical documentation and can be found freely downloadable at https://www.humanconnectome.org/study/hcp-young-adult/document/1200-subjects-data-release.

2.4.2. Image acquisition, fiber tracking and analysis

HCP data were acquired using a Siemens Skyra 3.0 T with a 32-
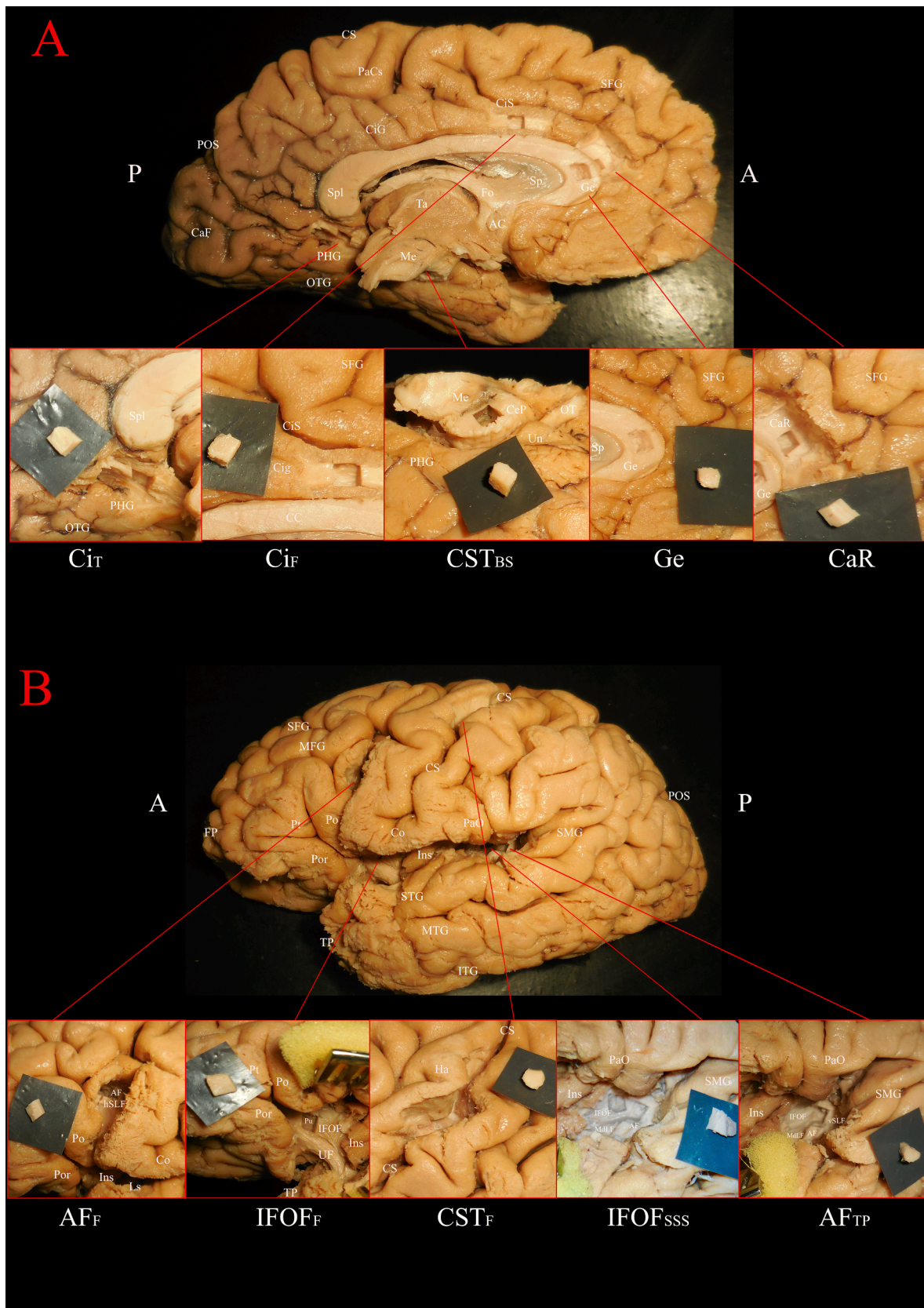
(caption on next page)

Fig. 1. A. The picture shows the anatomical location for the sampled region from the medial-ventral surface in a summary image (upper part) and in magnified details (lower part of A). A left hemisphere has been prepared with formalin fixation. The samples were collected with micro-knives and micro-dissectors. In the fronto-medial lobe two samples were collected from the fibers of the corpus callosum (Genu and callosal radiation, CaR) and one from the cingulum (Ci$_F$) at the level pre-supplementary motor area. In the temporo-occipital junction the temporal segment of the cingulum (Ci$_T$) was sampled once the cortex was removed from the medial portion of the parahippocampal gyrus (PHG). On the ventral surface, the anterior portion of the cerebral peduncle was sampled as a second segment of the cortico-spinal tract within the brainstem (CST$_{BS}$). B. The picture shows the anatomical landmarks for the samples collected from the lateral surface of this left hemisphere in a summary view (upper part of B) and in details with magnification through the microscope in the lower part. In the anterior region, the frontal segment of the arcuate fasciculus (AF) was identified after the dissection of the cortex of junction between the pars opercularis (Po) and the dorso-lateral prefrontal cortex. Once the u-fibers were removed, the horizontal segment of the superior longitudinal fasciculus was identified (hSLF). Medial in respect to the hSLF the AF fibers were exposed and sampled as AF$_F$. The limen insula was dissected at revealing the uncinate fasciculus (UF) and the inferior fronto-occipital fasciculus fibers running dorsally and medial within the external capsule. The IFOF was then sampled in the anterior portion revealing the putamen (Pu) exposed medial. The central sulcus (CS) was dissected at the level of the hand area revealing first u-fibers connecting the motor and sensory area for hand and then a vertical group of fibers deep running perpendicular to the bottom of the sulcus were sampled as CST fibers directed to the corona radiata and internal capsule (CST$_F$). The lateral sulcus (LS) was opened and the posterior insular region was identified. The medial portion of the superior temporal gyrus and supramarginal gyrus were removed to identify the perisilvian white matter. The vertical segment of the SLF (vSLF) was identified as more superficial/lateral in respect to the temporo-parietal portion of the AF fibers (AF$_{TP}$). Medially the fibers of the middle longitudinal fasciculus (MdLF) were identified running longitudinally from the sagittal stratum of Sachs (SSS) to the superior temporal gyrus (STG). More medial a group of longitudinal fibers running through the posterior portion of the external capsule were identified and sampled as IFOF$_{SSS}$.
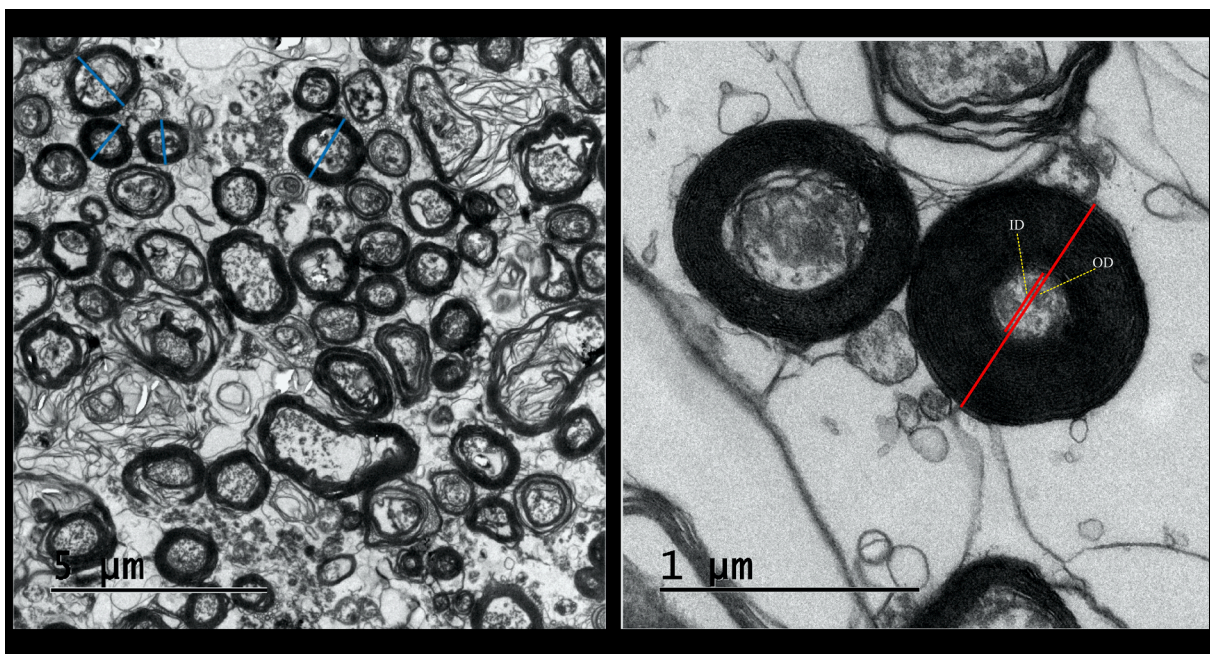

Fig. 2. Illustration of the interactive TEM image analysis of one CST$_{BS}$ sample. The left image shows one of several TEM images of the sample in which the myelinated fibers were measured (scalebar 5 μm). As a visual aid to avoid failing to measure some fibers, blue lines indicate fibers that have already been measured (see ESM1 for more information). The right image shows a myelinated fiber in the displayed close up (scalebar 1 μm) used for measuring the inner diameter (ID) and the outer diameter (OD). The g-ratio was automatically calculated by the software as presented in ESM1. (For interpretation of the references to color in this figure legend, the reader is referred to the web version of this article.)

channel head coil (Siemens Healthineers, Erlangen, Germany) according to the HCP Study Protocol (Van Essen et al., 2013). T1w image were acquired using the 3D MPRAGE sequence with 0.7 mm isotropic resolution (FOV = 224 mm, matrix = 320, 256 sagittal slices in a single slab), TR = 2400 ms, TE = 2.14 ms, TI = 1000 ms (Glasser et al., 2013). Diffusion data was acquired with a multi-shell diffusion scheme (b-values 1000, 2000, and 3000 s/mm^2), each shell with 90 diffusion sampling directions. The in-plane resolution and slice thickness were 1.25 mm, with TR = 5500 ms, TE = 89 ms, flip angle = 78 degrees using a multiband factor of 3.

All HCP diffusion datasets were pre-processed using the HCP MR Diffusion Pipeline (v3.19.0) which includes; EPI distortion correction using FSLs TOPUP algorithm, eddy current and motion correction using FSLs EDDY algorithm, gradient nonlinearity correction and calculation of b-value/b-vector deviation (Andersson et al., 2003; Andersson and Sotiropoulos, 2016; Sotiropoulos et al., 2013).

HCP diffusion data were reconstructed in DSI Studio (http://dsi-stud

io. labsolver.org) using the generalized q-sampling imaging approach (Yeh et al., 2010) with a diffusion distance ratio of 1.2. Prior to reconstruction, all included datasets were thoroughly examined to ensure the quality and integrity of diffusion data using the built-in quality control in DSI studio and by visual examination (Yeh et al., 2019).

We performed deterministic fiber tracking using DSI Studio software (DSI Studio, http://dsi-studio. labsolver.org/download-images), which utilizes a generalized streamline fiber tracking method (Yeh et al., 2013). The five selected white matter tracts were reconstructed in all the subjects following the anatomical criteria previously published with the Brain-Grid DTT reference atlas (Latini et al., 2019). Ten squared regions of interest (ROIs) were acquired matching the anatomical sampling criteria for TEM analysis for each hemisphere (Fig. 3) and the probabilistic infiltration weighted gradient maps for each group were matched for infiltration analysis. A total of 400 regions were acquired. DTI-based parameters including fractional anisotropy (FA), mean diffusivity (MD), axial diffusivity (AD) and radial diffusivity (RD) were acquired for each
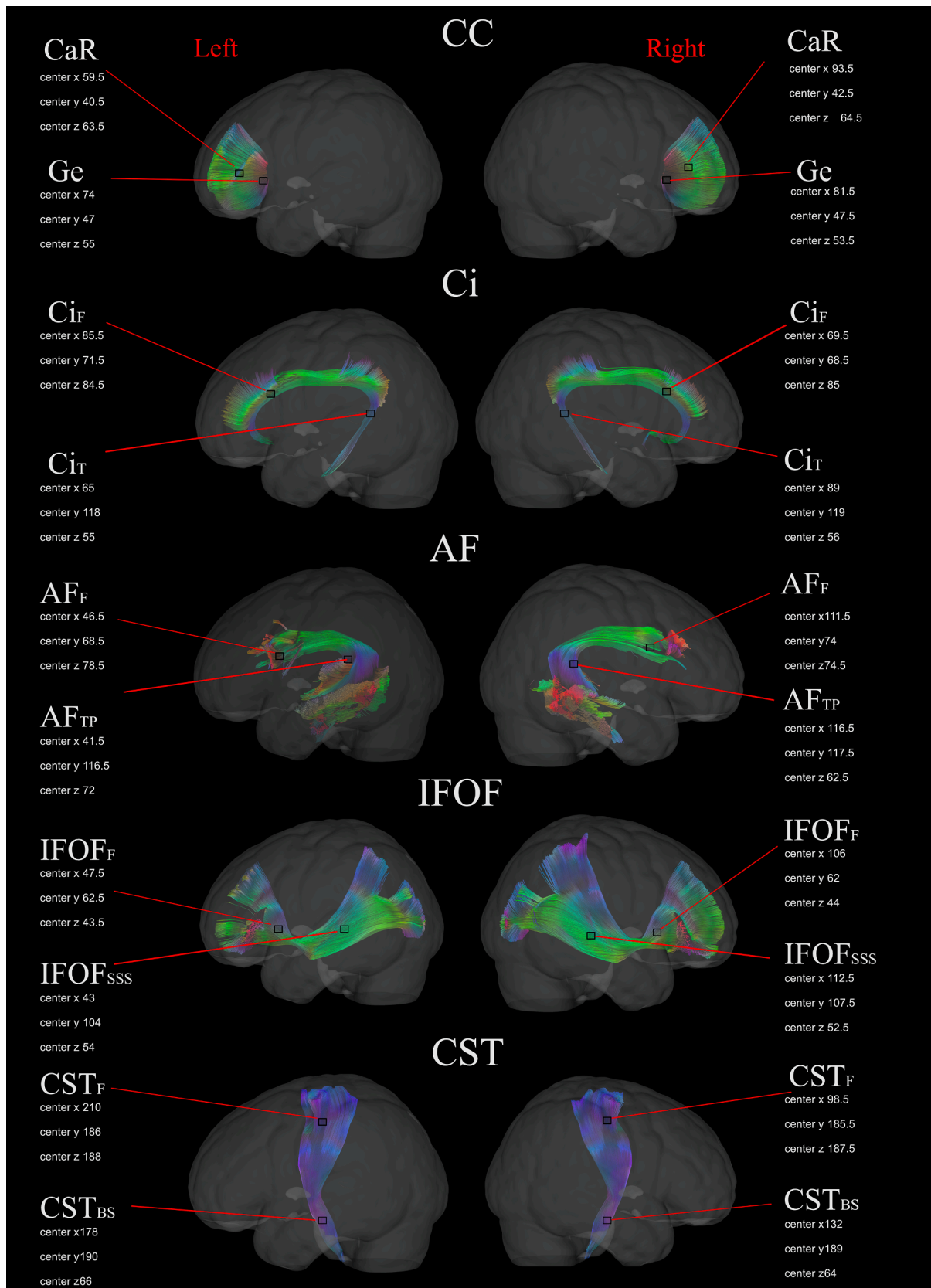
Fig. 3. The picture illustrates the position of the 20 region of interests (ROIs) analyzed in the 20 subjects from the HCP database (see ESM2 for more details). Two ROIs were collected for each white matter bundles for each side and based on the same anatomical criteria used for the TEM samples reflecting the different infiltration rate according to the probabilistic maps. For each ROI the MNI coordinates are provided (center x, y, z).

region and for each white matter bundle.

2.5. Statistical analysis

Descriptive statistics included mean and SD for both histological variables (the fiber density, inner diameter, outer diameter of fibers and g-ratio) and diffusion indices (FA, MD, AD, RD). The histological variables and the diffusion parameters were analyzed in two steps. First: white matter regions within the same bundles were compared with Kruskal Wallis test. Dunńs post-hoc test for multiple comparison was chosen as not parametric tests. Second, the sample regions were analyzed for the infiltration frequency in the three different groups: Astrocytomas IDHm, Astrocytomas IDHwt and Oligodendrogliomas. The median infiltration for each group was chosen as cut-off measure for further subgroup analysis. ROIs showing a mean infiltration higher than median were considered HIF, while those with mean infiltration lower than median were considered LIF. HIF and LIF groups were analyzed with Mann Whitney U test.

A Spearman correlation analysis was then used to detect relationship between diffusion parameters and infiltration risk. The Shapiro-Wilk test for normal distribution was performed and demonstrated normal and non-normal distribution among all variables, hence all statistical tests are performed as non-parametric. An effect size estimate (η^2) for Mann Whitney test was performed according to the formula: $\eta^2 = Z^2/N$ (where Z is the standard score and N is the sample size) (Coolican, 2018; Fritz et al., 2012). Statistical tests were performed at a significance level of P < .05. The statistical analysis was performed using the statistical package SPSS 25.0 (SPSS, Inc).

3. Results

3.1. White matter infiltration analysis

The tumor volume reconstruction of 67 patients with DLGG (25 IDHm astrocytomas, 16 IDHwt astrocytomas, and 26 oligodendrogliomas) was successfully merged into three probabilistic infiltration weighted gradient maps into MNI space based on their molecular status. The demographic and radiological features of the patients included in this study are summarized in Table 1 as a part of previously reported cohort (Latini et al., 2020a). The reconstruction of the 5 white matter pathways showed a clear difference in the infiltration within the same bundles in the three groups as displayed in Fig. 4.

IDHm astrocytomas infiltrated with higher frequency the fronto-temporal portion of IFOF, frontal portion of AF and CC on the left side. IDHwt astrocytomas displayed higher infiltration in the IFOF and AF on both sides predominant on their posterior extensions but also on the cingulum on the left side. Oligodendrogliomas showed a preferential infiltration of the frontal extension of the Ci, CC, IFOF and AF on both sides (Fig. 4). The frontal portion of IFOF (bilaterally) and the frontal portion of AF (left) were infiltrated with higher frequency in all the three groups.

The statistics of each ROI displayed the mean infiltration based on the infiltration gradient index for each group as displayed in Table 2. ROIs showing a mean infiltration higher than median were considered HIF, while those with mean infiltration lower than median value were considered LIF. AF_F on the left side and $IFOF_F$ bilaterally were than considered regions showing high infiltration frequency (HIF) in all the three groups, left Ge, right Ci_T, CST_{BS} bilaterally were considered regions with low infiltration frequency (LIF) in all the groups (Table 2). HIF and LIF regions were compared using the frequency of infiltration from the gradient map as variable showing significative difference in astrocytomas IDHm (p < .001), Astrocytomas IDHwt (p < .001) and Oligodendrogliomas (p < .001).

3.2. TEM measurements

A total number of 5509 fibers were measured in 100 white matter samples (mean 55.09, SD 17.20). No difference in the fiber density was detected among the different hemispheres (p 0.961). No difference in the fiber density was detected between left and right hemispheres (p 0.617). The fiber density, inner diameter, outer diameter, and g-ratio for each region are summarized in Table 3. First, we investigated morphological differences between regions of the same white matter bundles. The fiber density was significantly lower in the $IFOF_{SSS}$ compared with the $IFOF_F$. The fiber diameter (inner and/or outer) was significantly larger in the samples of the Ci_F, genu, $IFOF_{SSS}$ and CST_{BS}. The g-ratio was significantly lower in Ge, $IFOF_{SSS}$ and CST_{BS} compared with the respective counterpart (Table 4). The descriptive results for the complete white matter bundles are displayed in ESM3.

The 100 sample regions were analyzed according to the infiltration frequency for each group. In astrocytomas IDHm, HIF regions displayed a smaller inner (p < .001) and outer diameter (p < .001). In astrocytomas IDHwt, HIF regions showed smaller inner diameter (p < .05), outer diameter (p < .001) but also a larger g-ratio (p < .001). In the group of oligodendrogliomas, HIF regions displayed smaller inner and outer diameter (p < .001) (Table 5).

3.3. Diffusion parameters

The 400 analyzed ROIs sampled with the anatomical criteria used for TEM displayed a mean volume of 0.45 cm^3 (SD 0.13). The MNI co-ordinates for each region and the anatomical location are provided in Fig. 3. The descriptive results of each region according to the side are shown in Table 6.

Ge regions showed higher FA and lower MD-RD compared with callosal radiation. The Ci_F displayed a lower AD compared with the temporal region (p 0.006). The AF_F showed a lower FA and AD compared with the AF_{TP} region. The $IFOF_F$ presented lower FA, higher MD, and RD in respect to the $IFOF_{SSS}$. The CST_F displayed a lower MD and AD compared with the CST_{BS}. No other differences were detected among the white matter regions. The statistical results are displayed in Table 4. The descriptive results analyzing diffusion parameters for the

Table 1

Summary of the clinical, radiological data of the population divided in three groups according to the molecular status. Mol-confirmed: histological diagnosis (positive IDH-1–2 mutation for Astrocytomas, and IDH mutation and codeletion 1p19q for Oligodendrogliomas; negative IDH1-2 mutation implied IDH wild type status for astrocytomas). M: male subjects; F: female subjects; n: number; %: percentage within the same variable group; y: yes; n: no.

Clinical/Radiological factors	Astrocytomas-IDHm	Astrocytomas-IDHwt	Oligodendrogliomas
Number of patients	25	16	26
Age – Mean (SD)	39 (14)	42 (18)	41 (11)
Gender – m (%)/ f(%)	17 (68) / 8 (32)	5 (32) /11 (68)	16 (62) / 10 (38)
Epilepsy – y (%)/n (%)	20 (80) / 5 (20)	13 (82)/ 3 (18)	15 (58) /11(42)
Side of invasion – left (%)/ right (%)/ bilateral (%)	16 (64) / 8 (32) / 1 (4)	9 (56) / 6 (37) / 1 (7)	14 (54) / 11 (42)/ 1(4)
Radiological border – Sharp (%) / Diffuse (%)	10 (40) / 15 (60)	5 (32) /11 (68)	6 (23) / 20 (77)
Volume in ml – Mean (SD)	55.4 (52.3)	64.3 (54.6)	73.6 (55)

Fig. 4. The figure shows the probabilistic infiltration map obtained merging v the tumor volumes of 25 IDH mutant astrocytomas; 16 IDH wild type astrocytomas, and 26 Oligodendrogliomas [according to the WHO-2016 classification of brain tumors (Louis et al., 2016)] within MNI space. The genu of corpus callosum, the cingulum, the arcuate fasciculus, the inferior fronto-occipital fasciculus, and the cortico-spinal tract were reconstructed within the MNI space and merged with the gradient map for each subgroup. The right and the left side of the reconstructed white matter bundles are displayed within a glass-brain three-dimensional reconstruction. The color gradient with red spectrum indicates the higher frequency of infiltration per voxels for each subgroup (28% for the IDHm; 23% for the IDHwt, and 37% for the Oligodendrogliomas). (For interpretation of the references to color in this figure legend, the reader is referred to the web version of this article.)

Table 2

Summary of the different infiltration frequency for each analyzed group with average value and standard deviation (SD). The median infiltration frequency was 5% (range 0–28%) for Astrocytomas IDHm group, 3% for Astrocytomas IDHwt (range 0–23%) and 8% for Oligodendrogliomas (range 0–37%).

Regions	Astrocytomas IDHm			Astrocytomas IDHwt			Oligodendrogliomas		
	Average	SD	IF	Average	SD	IF	Average	SD	IF
Ge L	0.04	0.004	L	<0.00	0.002	L	0.08	0.009	L
Ge R	0.05	0.006	L	<0.00	0.002	L	0.13	0.01	H
Ca_R R	0.04	0.004	L	<0.00	<0.000	L	0.30	0.01	H
Ca_R L	0.14	0.01	H	<0.00	0.003	L	0.20	0.02	H
Ci_F L	0.02	0.014	L	0.07	0.005	H	0.08	0.02	L
Ci_F R	0.08	0.015	H	0.02	0.01	L	0.17	0.03	H
Ci_T L	<0.00	0.002	L	0.04	0.02	H	<0.00	<0.000	L
Ci_T R	0.02	0.006	L	0.02	0.009	L	0.02	0.007	L
AF_{TP} L	0.07	0.01	H	0.13	0.02	H	<0.00	<0.000	L
AF_F L	0.17	0.01	H	0.08	0.01	H	0.14	0.007	H
AF_F R	0.11	0.007	H	<0.00	0.002	L	0.24	0.02	H
AF_{TP} R	0.07	0.002	H	0.17	0.02	H	0.07	<0.000	L
$IFOF_{SSS}$ R	0.05	0.007	L	0.13	0.003	H	0.05	0.005	L
$IFOF_F$ R	0.07	0.01	H	0.06	0.009	H	0.11	0.005	H
$IFOF_F$ L	0.21	0.012	H	0.07	0.003	H	0.14	0.004	H
$IFOF_{SSS}$ L	0.11	0.006	H	0.18	0.019	H	0.04	0.013	L
CST_F L	<0.00	0.002	L	0.07	0.02	H	0.08	0.005	L
CST_F R	0.03	0.009	L	0.03	0.015	L	0.18	0.011	H
CST_{BS} R	<0.00	0.003	L	0.01	0.005	L	0.03	<0.000	L
CST_{BS} L	0.03	0.02	L	0.02	0.004	L	<0.00	0.003	L

For each group, regions with average infiltration higher than the median were considered with high (H) infiltration frequency (IF), while regions with average infiltration lower than the median were considered with low (L) infiltration frequency. Regions with high infiltration frequency (HIF) and low infiltration frequency (LIF) were then used for subgroup analysis.

complete white matter bundle are presented in ESM3.

A negative correlation ($r = -0.497$, $p = 0.026$) was found in the oligodendrogliomas group between infiltration frequency and AD. None of the other diffusion parameters were correlated with infiltration in the other two groups.

In the Astrocytomas IDHm group, the HIF regions showed lower FA ($p < .001$), lower AD ($p = .003$), and higher RD ($p < .001$) compared with LIF regions. In the Astrocytomas IDHwt group, HIF regions displayed lower FA ($p = .002$) and higher RD ($p = .015$) compared with LIF regions. In the oligodendrogliomas group, HIF regions showed lower FA, AD, and higher RD compared with LIF regions ($p < .001$) as shown in Table 5.

4. Discussion

Our study provided three main results. First, the infiltration analysis demonstrated clear regional differences in the infiltration frequency of five major white matter bundles in the three groups of DLGG. Second, regional differences within the same white matter bundles were detected by morphological analysis and diffusion parameter analysis. Third, regions with HIF displayed differences in histological and diffusion parameters compared with LIF regions among the analyzed subgroups.

4.1. Infiltration analysis

In this study we identified differences in the preferential regions affected by tumor infiltration among subgroups of diffuse gliomas. IDHm astrocytomas were mostly lateralized on the left fronto-temporal-sub insular region. The IDHwt astrocytomas displayed higher infiltration in the posterior temporal and temporo-parietal regions on both sides. The Oligodendrogliomas showed a tendency to infiltrate frontal subcortical regions on both sides. The "hotspots" for gliomas locations in the three groups were mostly subcortical (Latini et al., 2020a) including the different regions of white matter bundles and with possible different origins. Our results are in accordance with another recent study investigating the localization of DLGG according to the tumor molecular status. In this study, the authors found that IDH wild-type tumors are more often found near the sub-granular zone [hippocampus and dentate gyrus (Alvarez-Buylla et al., 2001)] than IDH mutated tumors (Skjulsvik

et al., 2020). This implied that IDH wild-type gliomas may reflect a different anatomical origin than IDH mutated astrocytomas and oligodendrogliomas (Skjulsvik et al., 2020). However, the authors did not investigate the white matter anatomy related to the preferential DG locations. Topographical differences in pathways of infiltration seem important to better understand the kinetics of gliomas, because they may recall some similarities with the mechanisms of cell migration during the developmental brain (Marín and Rubenstein, 2003; Olivier et al., 2001; Skjulsvik et al., 2020; Zhan et al., 2017). In fact, glioma cells actively migrate through extracellular spaces of the brain, and especially along white matter fibers, acting like non-malignant brain cells during embryonic development, or adult stem cells in the mature brain (Cuddapah et al., 2014). Once the tumor front cells reach the deep subcortical white matter, these tumors share similar pathways according to the original locations (Fathallah-Shaykh et al., 2019). These major pathways, seem to show a common pattern of infiltration which is not random or bidirectional but centripetal towards the central core and basal ganglia (Alfonso et al., 2017; Engwer et al., 2015; Painter and Hillen, 2013). This tendency to infiltrate regions close to basal ganglia was identified in our population enhancing regional differences within the same white matter bundles.

4.2. Regional differences within white matter bundles

We aimed to identify morphological and diffusion characteristics related to different white matter regions comparing TEM results and diffusion parameters. Our results suggest that there are morphological and diffusion differences between sampled areas of the major white matter bundles in the number of fibers, the diameter and g-ratio. In general fiber caliber is related to conduction velocity and in myelinated axons, conduction velocity increases approximately linearly with axon diameter (Gasser and Grundfest, 1939; Hursh, 1939). The g-ratio, equal to the ratio of the inner-to-outer diameter of a myelinated axon, is associated with the speed of conduction, and thus reflects axonal function and integrity. Hence, these morphological variables are also linked to a functional and evolutionary reasons (Chang et al., 2017; Edgar et al., 2020). In fact, it is convenient to increase the diameter of only those axons in which fast conduction velocity is relevant, e.g. for movement detection or for maintaining dynamical properties in large

Table 3

Summary of the histological variables analyzed with mean values and standard deviation (SD) for fiber density (from the formula: n fibers / examined area of 372 μm^2), for inner diameter, outer diameter, g-ratio in all the white matter samples for each side.

White matter regions	Variables	Left		Right	
		Mean	SD	Mean	SD
Ge	Fiber density	0.162	0.044	0.163	0.037
	Inner diameter	0.538	0.326	0.526	0.299
	Outer diameter	0.961	0.456	0.969	0.430
	g-ratio	0.514	0.172	0.536	0.111
Ca R	Fiber density	0.134	0.037	0.178	0.026
	Inner diameter	0.478	0.276	0.525	0.015
	Outer diameter	0.850	0.411	0.918	0.402
	g-ratio	0.553	0.125	0.557	0.113
Ci$_F$	Fiber density	0.137	0.036	0.153	0.055
	Inner diameter	0.579	0.301	0.530	0.262
	Outer diameter	0.980	0.434	0.933	0.382
	g-ratio	0.582	0.112	0.564	0.116
Ci$_T$	Fiber density	0.182	0.035	0.154	0.035
	Inner diameter	0.469	0.259	0.570	0.282
	Outer diameter	0.795	0.353	0.982	0.389
	g-ratio	0.576	0.119	0.573	0.122
AF$_{TP}$	Fiber density	0.124	0.018	0.174	0.091
	Inner diameter	0.619	0.371	0.535	0.293
	Outer diameter	1.051	0.478	0.937	0.419
	g-ratio	0.569	0.119	0.563	0.119
AF$_F$	Fiber density	0.144	0.068	0.144	0.065
	Inner diameter	0.600	0.375	0.479	0.282
	Outer diameter	1.049	0.517	0.858	0.381
	g-ratio	0.551	0.109	0.542	0.128
IFOF$_{SSS}$	Fiber density	0.124	0.022	0.109	0.028
	Inner diameter	0.525	0.272	0.584	0.343
	Outer diameter	0.936	0.383	0.992	0.466
	g-ratio	0.548	0.121	0.574	0.130
IFOF$_F$	Fiber density	0.172	0.046	0.185	0.015
	Inner diameter	0.535	0.280	0.518	0.286
	Outer diameter	0.902	0.400	0.837	0.371
	g-ratio	0.587	0.109	0.608	0.121
CST$_F$	Fiber density	0.143	0.016	0.113	0.023
	Inner diameter	0.569	0.339	0.553	0.317
	Outer diameter	0.990	0.457	0.952	0.427
	g-ratio	0.560	0.132	0.565	0.108
CST$_{BS}$	Fiber density	0.171	0.029	0.089	0.034
	Inner diameter	0.714	0.343	0.806	0.496
	Outer diameter	1.168	0.467	1.137	0.665
	g-ratio	0.601	0.108	0.562	0.131

Ge: Genu of corpus callosum; CaR: Callosal radiation; Ci$_F$: Frontal segment of cingulum; Ci$_T$: temporal segment of cingulum; AF$_{TP}$: temporo-parietal segment of arcuate fasciculus; AF$_F$: frontal segment of arcuate fasciculus; IFOF$_{SSS}$: longitudinal segment of inferior fronto-occipital fasciculus within the sagittal stratum of Sachs; CST$_F$: frontal segment of cortico-spinal tract (at the level of the hand area); CST$_{BS}$: Brain stem segment of the cortico-spinal tract at the level of the cerebral peduncle within the mesencephalon.

brain networks (Buzsáki et al., 2013). Larger fiber diameter in TEM results is linked to AD and FA in diffusion parameters (Lee et al., 2019; Tournier et al., 2011). AD refers to the diffusivity parallel with fiber tracts (Wheeler-Kingshott and Cercignani, n.d.; Winklewski et al., 2018). Lower AD may reflect reduced axonal caliber, or less coherent orientation of axons, i.e. obstacles hampering diffusion (Winklewski et al., 2018). On the other hand, FA refers to the fraction of diffusion that is directionally dependent (anisotropic). Lower FA might reflect in this case enlarged axonal diameter, reduced axonal packing density, or increased membrane permeability (Basser and Pierpaoli, 2011; Meoded et al., 2017). The g-ratio in our TEM results may reflect the observed variations of RD which refers, instead, to the diffusivity perpendicular to fiber tracts (Chang et al., 2017; Jung et al., 2018). RD may be relatively more sensitive to myelin, but higher RD might reflect myelin loss, or loss of axons and/or reduced axonal packing density (Winklewski et al., 2018).

In our study the fiber diameter was different between regions of the same bundles in 4 of the five analyzed tracts. However in the absence of concomitant difference in g-ratio or number of fibers the results were considered as related to the topographical variables/sampling of the white matter bundles as described by other authors (Giacci et al., 2018). IFOF and CST presented a more consistent difference between the two sampled regions in both TEM- and DTI parameters. The frontal portion of IFOF displayed higher number of fibers, a smaller fiber diameter and a higher myelin concentration. These differences may also match the lower FA and higher MD and RD presented by the frontal portion of IFOF. Even for CST, the frontal (dorsal) region displayed a smaller diameter (both inner and outer) but higher myelin thickness compared with the BS. The diffusion analysis demonstrated a significant lower MD and AD in the frontal portion. These results may be linked with a different organization of the fibers within the two regions with more organized and packed white matter fibers at the level of the brainstem reflecting higher MD and AD.

All together morphological features and diffusion proprieties seem to indicate that regional differences within the same pathways are associated with different topographical variables, such as coherent fiber orientation or packing of myelinated fibers. Differences within the same bundles may therefore be expected as suggested by other authors (Giacci et al., 2018; Lee et al., 2019). These differences seem also indicating a consistent topographical variability. In fact, regions within the limbic system (frontal-fronto/mesial, sub-insular /insular) which synchronize large scale networks, display larger extracellular space, higher myelin contents and high connectivity (Bartzokis et al., 2001; Coelho et al., 2021; Fields, 2008).

4.3. HIF regions vs LIF regions

Analyzed by infiltration frequency, HIF regions consistently presented a smaller inner and outer diameter in the three analyzed groups. IDHwt Astrocytomas only, displayed a lower myelin concentration in

Table 4

Summary of the statistical results comparing the white matter regions within the same bundles for all the variables analysed. Kruskal Wallis test was used for comparison among the white matter regions with test significance for p < .05. The displayed values are adjusted with Dunńs multiple comparison correction test.

White matter regions	Fibre density	Inner diameter	Outer diameter	g-ratio	FA	MD	AD	RD
	p	p	p	p	p	p	p	p
Genu vs CaR	1.000	0.269	0.000*	0.007*	0.000*	0.000*	0.999	0.000*
Ci$_F$ vs Ci$_T$	1.000	0.041*	0.004*	0.999	0.999	0.999	0.006*	0.999
AF$_F$ vs AF$_{TP}$	1.000	0.099	0.340	0.055	0.007*	0.266	0.000*	0.224
IFOF$_F$ vs IFOF$_{SSS}$	0.025*	0.795	0.000*	0.000*	0.000*	0.000*	0.999	0.000*
CST$_F$ vs CST$_{BS}$	1.000	0.000*	0.000*	0.004*	0.999	0.045*	0.000*	0.999

Ge: Genu of corpus callosum; CaR: Callosal radiation; Ci$_F$: Frontal segment of cingulum; Ci$_T$: temporal segment of cingulum; AF$_{TP}$: temporo-parietal segment of arcuate fasciculus; AF$_F$: frontal segment of arcuate fasciculus; IFOF$_{SSS}$: longitudinal segment of inferior fronto-occipital fasciculus within the sagittal stratum of Sachs; CST$_F$: frontal segment of cortico-spinal tract (at the level of the hand area); CST$_{BS}$: Brain stem segment of the cortico-spinal tract at the level of the cerebral peduncle within the mesencephalon.

Table 5

Summary of the TEM results and DTI results for regions with high frequency of infiltration (HIF) and region with low frequency of infiltration (LIF) in Astrocytomas IDH mutant (A-IDHm), Astrocytomas IDHwt (A-IDHwt) and Oligodendrogliomas (Oligo). Mann Whitney U test was used for comparison between the two groups with significant results (*) with $p < 0.05$ and 95% Confidence interval; η^2 shows the effect size estimate according to Fritz et al. (Fritz et al., 2012). Interpretation of the sample size estimate is a large effect is 0.5, a medium effect is 0.3, and a small effect is 0.1. (Coolican, 2018; Fritz et al., 2012).

TEM

Groups	IF	FD	SD	p	η^2	ID	SD	η^2	OD	SD	p	η^2	g-ratio	SD	p	η^2
A-IDHm	LIF	0.145	0.041	0.739	0.043	0.575	0.332	0.018	0.991	0.461	<0.001*	0.071	0.563	0.126	0.499	0.000
	HIF	0.150	0.052			0.534	0.303		0.924	0.421			0.567	0.120		
A-IDHwt	LIF	0.146	0.045	0.989	0.000	0.564	0.326	0.000	0.985	0.456	<0.001*	0.006	0.556	0.121	<0.001*	0.021
	HIF	0.149	0.045			0.548	0.313		0.937	0.433			0.573	0.120		
Oligo	LIF	0.142	0.045	0.241	0.013	0.582	0.336	0.082	0.999	0.446	<0.001*	0.190	0.566	0.128	0.219	0.013
	HIF	0.154	0.046			0.527	0.297		0.917	0.417			0.564	0.118		

DTI

Groups	IF	FA	SD	p	η^2	MD	SD	p	η^2	AD	SD	p	η^2	RD	SD	p	η^2
A-IDHm	LIF	0.729	0.126	<0.001*	0.059	0.216	0.059	0.110	0.006	0.400	0.076	0.003*	0.015	0.104	0.056	<0.001*	0.044
	HIF	0.660	0.112			0.221	0.055			0.383	0.068			0.123	0.044		
A-IDHwt	LIF	0.717	0.142	0.002*	0.007	0.216	0.055	0.325	0.002	0.398	0.066	0.437	0.000	0.106	0.055	0.015*	0.014
	HIF	0.680	0.102			0.220	0.060			0.386	0.079			0.119	0.048		
Oligo	LIF	0.729	0.115	<0.001*	0.082	0.217	0.060	0.360	0.002	0.402	0.077	<0.001*	0.04	0.105	0.053	<0.001*	0.039
	HIF	0.660	0.124			0.220	0.055			0.381	0.067			0.122	0.049		

IF: infiltration frequency; FD: fiber density; SD: standard deviation; ID: inner diameter; OD: outer diameter; FA: fractional anisotropy; MD: mean diffusivity; AD: axial diffusivity; RD: radial diffusivity.

Table 6

Summary of the descriptive results from analysis of the diffusion indices for each white matter region analyzed in this study.

White matter regions	Parameters	Left		Right	
		Mean	SD	Mean	SD
Ge	FA	0.904	0.030	0.906	0.024
	MD	0.155	0.018	0.157	0.016
	AD	0.391	0.041	0.398	0.039
	RD	0.036	0.012	0.036	0.009
CaR	FA	0.714	0.049	0.626	0.059
	MD	0.202	0.022	0.216	0.024
	AD	0.397	0.029	0.381	0.041
	RD	0.104	0.022	0.133	0.024
Ci_F	FA	0.577	0.060	0.521	0.061
	MD	0.231	0.030	0.249	0.020
	AD	0.388	0.034	0.393	0.024
	RD	0.152	0.030	0.178	0.024
Ci_T	FA	0.569	0.060	0.592	0.057
	MD	0.275	0.049	0.256	0.038
	AD	0.431	0.054	0.435	0.042
	RD	0.197	0.048	0.167	0.039
AF_{TP}	FA	0.765	0.046	0.708	0.061
	MD	0.195	0.019	0.216	0.024
	AD	0.411	0.046	0.422	0.032
	RD	0.086	0.017	0.104	0.024
AF_F	FA	0.035	0.375	0.543	0.074
	MD	0.154	0.022	0.229	0.030
	AD	0.287	0.038	0.363	0.028
	RD	0.088	0.017	0.163	0.035
$IFOF_{SSS}$	FA	0.826	0.054	0.747	0.048
	MD	0.178	0.038	0.217	0.031
	AD	0.399	0.063	0.444	0.055
	RD	0.067	0.027	0.104	0.024
$IFOF_F$	FA	0.601	0.033	0.571	0.044
	MD	0.240	0.019	0.254	0.025
	AD	0.430	0.032	0.430	0.036
	RD	0.145	0.016	0.167	0.023
CST_F	FA	0.745	0.059	0.772	0.046
	MD	0.154	0.030	0.202	0.026
	AD	0.316	0.051	0.428	0.036
	RD	0.073	0.022	0.089	0.022
CST_{BS}	FA	0.800	0.039	0.793	0.030
	MD	0.190	0.018	0.216	0.026
	AD	0.440	0.032	0.460	0.050
	RD	0.065	0.016	0.094	0.016

Ge: Genu of corpus callosum; CaR: Callosal radiation; Ci_F: Frontal segment of cingulum; Ci_T: temporal segment of cingulum; AF_{TP}: temporo-parietal segment of arcuate fasciculus; AF_F: frontal segment of arcuate fasciculus; $IFOF_{SSS}$: longitudinal segment of inferior fronto-occipital fasciculus within the sagittal stratum of Sachs; CST_F: frontal segment of cortico-spinal tract (at the level of the hand area); CST_{BS}: Brain stem segment of the cortico-spinal tract at the level of the cerebral peduncle within the mesencephalon.

HIF regions. DTI analysis indicated that HIF regions in all the three groups present a lower FA and higher RD in respect with LIF regions. In IDHm astrocytomas and oligodendrogliomas, HIF regions displayed also a lower AD compared with LIF regions. The smaller diameter with lower myelin concentration may suggest two different considerations. First, the invasion of glioma cells into the adjacent brain tissue is guided by a combination of multiple molecular and physical mechanisms along pre-existing tracks of least resistance (Cuddapah et al., 2014). The major invasion routes are basement membranes and intercellular tracks provided by myelinated axons and astrocyte processes (Mathiisen et al., 2010; Wolburg et al., 2009). Larger extracellular space between fibers may be therefore facilitate tumor cells becoming a pathway of least resistance for dissemination (Alfonso et al., 2017; Berens and Giese, 1999; Cuddapah et al., 2014). Second, the presence of lower myelin content in HIF regions only in the IDHwt astrocytomas may possibly depend on the the different localization of the IDHwt tumors. Compared with the other two groups IDHwt astrocytomas were located more posteriorly involving both association and projection pathways. Posterior temporal and temporo-parietal regions are characterized by a

different myelination process during life (Billiet et al., 2015; Cercignani et al., 2017) and therefore by the different white matter aging process compared with other regions or pathways (Bartzokis et al., 2012; Billiet et al., 2015; Cercignani et al., 2017). However, since the IDHwt status and specific tumor location have been linked to a different gliogenesis and prognosis (Skjulsvik et al., 2020), we are not able to exclude a possible genetic link between IDHwt status and specific white matter features as suggested for other genes (Hatton et al., 2018). Moreover, the three groups displayed lower FA and higher RD in HIF regions. These results suggest a possible enlarged extra-axonal space or a decrease in myelin content in HIF regions (Basser and Pierpaoli, 2011; Tournier et al., 2011; Wheeler-Kingshott and Cercignani, 2009; Winklewski et al., 2018). These results seem not to be influenced by the different preferential locations of the different subgroups and in agreement with the histological features detected by TEM analysis (smaller fiber caliber).

The lower AD detected in HIF regions for IDHm astrocytomas and oligodendrogliomas may represent a measure of less coherent organization of white matter tracts and probably linked with the specific anterior location (Alexander et al., 2011; Kumar et al., 2012; Wheeler-Kingshott and Cercignani, 2009). This seems to be related to regions with higher number of crossing fibers (i.e. fronto-orbital region, deep frontal regions) rather than those with packed myelinated fibers (such as SSS or BS). Another possibility is that, the lower AD in our population (IDHm astrocytomas and Oligodendrogliomas) may result from the increased numbers of brain fibers in those areas of late myelination, allowing fibers to become less straight due to reduced inter-axonal space (Mukherjee et al., 2002; Qiu et al., 2008; Suzuki et al., 2003; Wheeler-Kingshott and Cercignani, 2009). This may also explain why IDHwt astrocytomas located in posterior regions did not show the same trend.

Merging our results with the theories on glioma cells migration, we may hypothesize that in all three groups of DLGG, the smaller fiber diameter (inner and outer diameter), increased extracellular space or decreased fiber density (higher RD) in areas with high functional demand (Coelho et al., 2021; Fields, 2008) but sensitive for microstructural changes (lower FA) may represent permissive environmental factors for gliomas cells to go or grow (Alfonso et al., 2017; Burgess et al., 1997; Engwer et al., 2015).

4.4. Limitations

Our study has some limitations and therefore the results presented herein should be interpreted with caution. First, the age of the subjects in the three groups was quite different due to technical and practical constraints. It is known that the human white matter is among the most vulnerable tissues during the aging process, especially in late-myelinating regions, such as frontal and temporal lobes (Bartzokis et al., 2001; Cercignani et al., 2017). In fact, latest myelinated regions display a decrease in FA with older age which seems to be due to increased axonal dispersion rather than demyelination (Billiet et al., 2015; Hsu et al., 2010). The older age of the cadaver donors may have influenced the histological results and the correlation between histological parameters and diffusion parameters may be different analyzing samples from younger brains specimens. However, since the other two groups (patients and healthy subjects) were closer in the mean age and the histological results were interpreted based on the distribution of tumors merging multiple techniques, we believe that the influence of the so called antero-posterior gradient of retrogenesis (Bartzokis et al., 2012; Billiet et al., 2015; Cercignani et al., 2017) would not crucially affect the interpretation of the overall study. Second, the probabilistic infiltration analysis of the different subgroups was limited by the numbers of patients included. Only 67 patients had a confirmed molecular status according to WHO-2016 classification and to improve the impact of this study patients with incomplete molecular status were excluded. Hence, only larger cohorts of molecularly confirmed gliomas may corroborate our results on differences in white matter infiltration among the three subgroups.

Third, the specimens used for the white matter dissection and collection, were only formalin fixated but not prepared for the standard revised Klingleŕs protocol as previously described (Latini et al., 2020b, 2017, 2015). The choice was dictated by the possible effect of the freezing process on fibers' morphology (Zemmoura et al., 2016). The consequence of this choice is that some regions such as fronto-opercular area, sagittal stratum of Sachs were not perfectly prepared for the blunt dissection. Differences in the exposure of the white matter structures may result from the different specimens. However, the samples were collected in a standardized way by a neurosurgeon with experience on white matter dissection, minimizing the risk of collecting wrong structures.

Fourth, we need to address limitations related to the sample preparation and measurement using TEM. The PMI interval was not optimal in two hemispheres, fixated within 48 and 72 h after death. This may have possibly affected the qualitative results but since the number of the myelinated fibers did not change among the hemispheres and samples we believe that our results may be considered consistent. Moreover, we could not identify unmyelinated axons with certainty in our specimens, due to disintegration after late fixation. All our measurements, then, were made on myelinated axons only so the number of unmyelinated axons may also be a factor affecting differences in HIF and LIF regions. Fifth, differences in the g-ratio measures among regions may be due to the difference of changes in myelin structures during the EM preparation (Kirschner and Hollingshead, 1980), such as fixation and dehydration, and potentially inaccurate segmentation of the myelin sheath.

Sixth, the choice of analyzing only 5 white matter bundles may lead to incomplete results because not all the possible regions were tested (e. g. occipital lobe). However we chose fiber bundles already analyzed in literature with TEM techniques and our descriptive results are in agreement with other authors regarding the mean fiber diameter and g-ratio (Benjamini et al., 2016; Cercignani et al., 2017; Liewald et al., 2014). To increase reliability, we sampled two different regions from the same white matter structures based on our preliminary results on the infiltration frequency and for this reason two samples were considered to possibly increase the reliability of the results.

Seventh, the creation of the ROIs /samples for diffusion analysis was performed based on anatomical criteria used for the samples collection on cadaver specimens. Some variations in the position and the volume of the regions cannot be excluded but the we believe that we have provided all the information to increase reproducibility of this study.

Finally, due to the retrospective nature of this study and the long-time span differences in image resolution parameters were unavoidable. That being said, the different resolution could be a potential limitation. Partial volume effects, especially in low resolution planes may induced over- or underestimation of the tumor boundary definition during segmentation. The preferential locations of DLGG given by the infiltration segmentation were used to define white matter pathways that were commonly infiltrated and not commonly infiltrated. In that sense, partial volume effects should not compromise the selection of these white matter pathways due to small effects that are averaged out in the template since several DLGG with different locations are added.

4.5. Future perspectives

Aware of the limitations stated above, our study represents an original effort to investigate morphological white matter features, diffusion parameters and gliomas infiltration frequency in three different subgroups of molecularly confirmed gliomas. Due to the retrospective nature of the study on a cohort enrolled in 15 years, we believe that we have provided a new possible method to investigate the white matter/ gliomas interaction. Only future studies would be able to corroborate our results. A possible improvements would be to enroll homogeneous groups of patients and controls with same age; analyzing them with preoperative DTI (possibly reconstructing several white matter bundles) and multimodal imaging to characterize white matter

features (Alexander et al., 2011; Bartzokis et al., 2012; Cercignani et al., 2017); then acquiring samples during tumor resection (for TEM and immuno-histochemical analyses) spatially registered to navigation system to increase consistency between the different techniques. In this way we might be able to better understand wheatear a correlation between morphological, pathological and diffusion parameters exist in DLGG.

5. Conclusions

We identified differences in the preferential white matter infiltration of five major white matter bundles in three groups of DLGG. IDHm astrocytomas had the tendency to infiltrate fronto-temporal subcortical areas on the left side. IDHwt astrocytomas were preferentially located in the posterior-temporal and temporo-parietal regions of both sides. Oligodendrogliomas infiltrated anterior subcortical regions of the frontal lobes of both sides.

We also identified regional differences within the same pathways possibly associated with different topographical variables, such as coherent fiber orientation or packing of myelinated fibers. Our multimodal analysis showed that common regions with high infiltration frequency (HIF) displayed a smaller fiber diameter, lower FA and higher RD compared with low infiltration frequency (LIF) regions. Our results may indicate that both morphological features and diffusion parameters of the white matter fibers are different in regions linked to the preferential location of DLGG.

6. Data and code availability statement

MRI data from the original study that support the findings are available on request from the corresponding author. The data are not publicly available due to privacy or ethical restrictions. The source code of the "Parameters measurement software" has been made freely available at https://github.com/AndreaBehan/White_matter_annotation_software under the MIT License. The data analysis from the electron microscopy investigation is available at SciLifelab depository (DOI https://doi.org//10.17044/scilifelab.14047457).

CRediT authorship contribution statement

Francesco Latini: Conceptualization, Methodology, Formal analysis, Writing - original draft, Visualization, Validation, Writing - review & editing. **Markus Fahlström:** Investigation, Methodology, Formal analysis, Data curation, Writing - review & editing. **Andrea Beháňová:** Methodology, Software, Data curation, Writing - review & editing. **Ida-Maria Sintorn:** Methodology, Software, Data curation, Writing - review & editing. **Monika Hodik:** Investigation, Methodology, Data curation, Writing - review & editing. **Karin Staxäng:** Investigation, Methodology, Data curation, Writing - review & editing. **Mats Ryttlefors:** Conceptualization, Methodology, Supervision, Project administration, Resources, Writing - review & editing.

Dissertation

Preliminary results of this study has been published as doctorate thesis dissertation entitled "Significance of white matter anatomy in interpreting features and behaviour of low-grade gliomas and implications for surgical treatment", published by Uppsala: Acta Universitatis Upsaliensis, 2021. Digital Comprehensive Summaries of Uppsala Dissertations from the Faculty of Medicine, ISSN 1651-6206; 1744. urn: nbn:se:uu:diva-439624.

Declaration of Competing Interest

The authors declare that they have no known competing financial interests or personal relationships that could have appeared to influence the work reported in this paper.

Appendix A. Supplementary data

Supplementary data to this article can be found online at https://doi.org/10.1016/j.nicl.2021.102735.

References

Alexander, A.L., Hurley, S.A., Samsonov, A.A., Adluru, N., Hosseinbor, A.P., Mossahebi, P., Tromp, D.P.M., Zakszewski, E., Field, A.S., 2011. Characterization of cerebral white matter properties using quantitative magnetic resonance imaging stains. Brain Connect. 1 (6), 423–446. https://doi.org/10.1089/brain.2011.0071.

Alfonso, J.C.L., Talkenberger, K., Seifert, M., Klink, B., Hawkins-Daarud, A., Swanson, K. R., Hatzikirou, H., Deutsch, A., 2017. The biology and mathematical modelling of glioma invasion: a review. J. R. Soc. Interface 14 (136), 20170490. https://doi.org/10.1098/rsif.2017.0490.

Alvarez-Buylla, A., García-Verdugo, J.M., Tramontin, A.D., 2001. A unified hypothesis on the lineage of neural stem cells. Nat. Rev. Neurosci. 2 (4), 287–293. https://doi.org/10.1038/35067582.

Andersson, J.L.R., Skare, S., Ashburner, J., 2003. How to correct susceptibility distortions in spin-echo echo-planar images: application to diffusion tensor imaging. Neuroimage 20 (2), 870–888. https://doi.org/10.1016/S1053-8119(03)00336-7.

Andersson, J.L.R., Sotiropoulos, S.N., 2016. An integrated approach to correction for off-resonance effects and subject movement in diffusion MR imaging. Neuroimage 125, 1063–1078. https://doi.org/10.1016/j.neuroimage.2015.10.019.

Bartzokis, G., Beckson, M., Lu, P.H., Nuechterlein, K.H., Edwards, N., Mintz, J., 2001. Age-related changes in frontal and temporal lobe volumes in men: a magnetic resonance imaging study. Arch. Gen. Psychiatry 58 (5), 461. https://doi.org/10.1001/archpsyc.58.5.461.

Bartzokis, G., Lu, P.H., Heydari, P., Couvrette, A., Lee, G.J., Kalashyan, G., Freeman, F., Grinstead, J.W., Villablanca, P., Finn, J.P., Mintz, J., Alger, J.R., Altshuler, L.L., 2012. Multimodal magnetic resonance imaging assessment of white matter aging trajectories over the lifespan of healthy individuals. Biol. Psychiatry Dev. Autism Aggression 72 (12), 1026–1034. https://doi.org/10.1016/j.biopsych.2012.07.010.

Basser, P.J., Pierpaoli, C., 2011. Microstructural and physiological features of tissues elucidated by quantitative-diffusion-tensor MRI. 1996. J. Magn. Reson. 213 (2), 560–570. https://doi.org/10.1016/j.jmr.2011.09.022.

Benjamini, D., Komlosh, M.E., Holtzclaw, L.A., Nevo, U., Basser, P.J., 2016. White matter microstructure from nonparametric axon diameter distribution mapping. Neuroimage 135, 333–344. https://doi.org/10.1016/j.neuroimage.2016.04.052.

Berens, M.E., Giese, A., 1999. "…those left behind". Biology and oncology of invasive glioma cells. Neoplasia 1 (3), 208–219.

Billiet, T., Vandenbulcke, M., Mädler, B., Peeters, R., Dhollander, T., Zhang, H., Deprez, S., Van den Bergh, B.R.H., Sunaert, S., Emsell, L., 2015. Age-related microstructural differences quantified using myelin water imaging and advanced diffusion MRI. Neurobiol. Aging 36 (6), 2107–2121. https://doi.org/10.1016/j.neurobiolaging.2015.02.029.

Burgess, P.K., Kulesa, P.M., Murray, J.D., Alvord, E.C., 1997. The interaction of growth rates and diffusion coefficients in a three-dimensional mathematical model of gliomas. J. Neuropathol. Exp. Neurol. 56 (6), 704–713.

Buzsáki, G., Logothetis, N., Singer, W., 2013. Scaling brain size, keeping timing: evolutionary preservation of brain rhythms. Neuron 80, 751–764. https://doi.org/10.1016/j.neuron.2013.10.002.

Capper, D., Zentgraf, H., Balss, J., Hartmann, C., von Deimling, A., 2009. Monoclonal antibody specific for IDH1 R132H mutation. Acta Neuropathol. 118 (5), 599–601. https://doi.org/10.1007/s00401-009-0595-z.

Cercignani, M., Giulietti, G., Dowell, N.G., Gabel, M., Broad, R., Leigh, P.N., Harrison, N. A., Bozzali, M., 2017. Characterizing axonal myelination within the healthy population: a tract-by-tract mapping of effects of age and gender on the fiber g-ratio. Neurobiol. Aging 49, 109–118. https://doi.org/10.1016/j.neurobiolaging.2016.09.016.

Chang, E.H., Argyelan, M., Aggarwal, M., Chandon, T.-S.-S., Karlsgodt, K.H., Mori, S., Malhotra, A.K., 2017. The role of myelination in measures of white matter integrity: combination of diffusion tensor imaging and two-photon microscopy of CLARITY intact brains. Neuroimage 147, 253–261. https://doi.org/10.1016/j.neuroimage.2016.11.068.

Coelho, A., Fernandes, H.M., Magalhães, R., Moreira, P.S., Marques, P., Soares, J.M., Amorim, L., Portugal-Nunes, C., Castanho, T., Santos, N.C., Sousa, N., 2021. Signatures of white-matter microstructure degradation during aging and its association with cognitive status. Sci. Rep. 11, 4517. https://doi.org/10.1038/s41598-021-83983-7.

Coolican, H., 2018. Research Methods and Statistics in Psychology. Routledge.

Cuddapah, V.A., Robel, S., Watkins, S., Sontheimer, H., 2014. A neurocentric perspective on glioma invasion. Nat. Rev. Neurosci. 15 (7), 455–465. https://doi.org/10.1038/nrn3765.

Duffau, H., Capelle, L., 2004. Preferential brain locations of low-grade gliomas. Cancer 100 (12), 2622–2626. https://doi.org/10.1002/(ISSN)1097-014210.1002/cncr.v100:1210.1002/cncr.20297.

Edgar, J.M., Smith, R.S., Duncan, I.D., 2020. Transmission Electron Microscopy and Morphometry of the CNS White Matter. In: Babetto, E. (Ed.), Axon Degeneration: Methods and Protocols, Methods in Molecular Biology. Springer US, New York, NY, pp. 233–261. https://doi.org/10.1007/978-1-0716-0585-1_18.

Elsir, T., Qu, M., Berntsson, S.G., Orrego, A., Olofsson, T., Lindström, M.S., Nistér, M., von Deimling, A., Hartmann, C., Ribom, D., Smits, A., 2011. PROX1 is a predictor of survival for gliomas WHO grade II. Br. J. Cancer 104 (11), 1747–1754. https://doi.org/10.1038/bjc.2011.162.

Engwer, C., Hillen, T., Knappitsch, M., Surulescu, C., 2015. Glioma follow white matter tracts: a multiscale DTI-based model. J. Math. Biol. 71 (3), 551–582. https://doi.org/10.1007/s00285-014-0822-7.

Fathallah-Shaykh, H.M., DeAtkine, A., Coffee, E., Khayat, E., Bag, A.K., Han, X., Warren, P.P., Bredel, M., Fiveash, J., Markert, J., Bouaynaya, N., Nabors, L.B., De Nunzio, G., 2019. Diagnosing growth in low-grade gliomas with and without longitudinal volume measurements: a retrospective observational study. PLoS Med. 16 (5), e1002810. https://doi.org/10.1371/journal.pmed.1002810.

Fields, R.D., 2008. White matter in learning, cognition and psychiatric disorders. Trends Neurosci. 31 (7), 361–370. https://doi.org/10.1016/j.tins.2008.04.001.

Fritz, C.O., Morris, P.E., Richler, J.J., 2012. Effect size estimates: current use, calculations, and interpretation. J. Exp. Psychol. Gen. 141, 2–18. https://doi.org/10.1037/a0024338.

Gasser, H.S., Grundfest, H., 1939. Axon diameters in relation to the spike dimensions and the conduction velocity in mammalian a fibers. Am. J. Physiol.-Legacy Content 127, 393–414. https://doi.org/10.1152/ajplegacy.1939.127.2.393.

Giacci, M.K., Bartlett, C.A., Huynh, M., Kilburn, M.R., Dunlop, S.A., Fitzgerald, M., 2018. Three dimensional electron microscopy reveals changing axonal and myelin morphology along normal and partially injured optic nerves. Sci. Rep. 8, 3979. https://doi.org/10.1038/s41598-018-22361-2.

Glasser, M.F., Sotiropoulos, S.N., Wilson, J.A., Coalson, T.S., Fischl, B., Andersson, J.L., Xu, J., Jbabdi, S., Webster, M., Polimeni, J.R., Van Essen, D.C., Jenkinson, M., 2013. The minimal preprocessing pipelines for the Human Connectome Project. NeuroImage Mapping Connectome 80, 105–124. https://doi.org/10.1016/j.neuroimage.2013.04.127.

Hatton, S.N., Panizzon, M.S., Vuoksimaa, E., Hagler, D.J., Fennema-Notestine, C., Rinker, D., Eyler, L.T., Franz, C.E., Lyons, M.J., Neale, M.C., Tsuang, M.T., Dale, A. M., Kremen, W.S., 2018. Genetic relatedness of axial and radial diffusivity indices of cerebral white matter microstructure in late middle age. Hum. Brain Mapp. 39 (5), 2235–2245. https://doi.org/10.1002/hbm.v39.510.1002/hbm.24002.

Hsu, J.-L., Van Hecke, W., Bai, C.-H., Lee, C.-H., Tsai, Y.-F., Chiu, H.-C., Jaw, F.-S., Hsu, C.-Y., Leu, J.-G., Chen, W.-H., Leemans, A., 2010. Microstructural white matter changes in normal aging: a diffusion tensor imaging study with higher-order polynomial regression models. NeuroImage 49 (1), 32–43. https://doi.org/10.1016/j.neuroimage.2009.08.031.

Hursh, J.B., 1939. Conduction velocity and diameter of nerve fibers. Am. J. Physiol.-Legacy Content 127, 131–139. https://doi.org/10.1152/ajplegacy.1939.127.1.131.

Ius, T., Angelini, E., Thiebaut de Schotten, M., Mandonnet, E., Duffau, H., 2011. Evidence for potentials and limitations of brain plasticity using an atlas of functional resectability of WHO grade II gliomas: towards a "minimal common brain". Neuroimage 56 (3), 992–1000. https://doi.org/10.1016/j.neuroimage.2011.03.022.

Jakola, A.S., Myrmel, K.S., Kloster, R., Torp, S.H., Lindal, S., Unsgård, G., Solheim, O., 2012. Comparison of a strategy favoring early surgical resection vs a strategy favoring watchful waiting in low-grade gliomas. JAMA 308, 1881–1888. https://doi.org/10.1001/jama.2012.12807.

Jakola, A.S., Unsgård, G., Myrmel, K.S., Kloster, R., Torp, S.H., Losvik, O.K., Lindal, S., Solheim, O., 2013. Surgical strategy in grade II astrocytoma: a population-based analysis of survival and morbidity with a strategy of early resection as compared to watchful waiting. Acta Neurochir. (Wien) 155 (12), 2227–2235. https://doi.org/10.1007/s00701-013-1869-8.

Jakola, A.S., Unsgård, G., Myrmel, K.S., Kloster, R., Torp, S.H., Sagberg, L.M., Lindal, S., Solheim, O., 2014. Surgical strategies in low-grade gliomas and implications for long-term quality of life. J. Clin. Neurosci. 21 (8), 1304–1309. https://doi.org/10.1016/j.jocn.2013.11.027.

Jung, W., Lee, J., Shin, H.-G., Nam, Y., Zhang, H., Oh, S.-H., Lee, J., 2018. Whole brain g-ratio mapping using myelin water imaging (MWI) and neurite orientation dispersion and density imaging (NODDI). Neuroimage 182, 379–388. https://doi.org/10.1016/j.neuroimage.2017.09.053.

Kansal, A.R., Torquato, S., Harsh, G.R., Chiocca, E.A., Deisboeck, T.S., 2000. Simulated brain tumor growth dynamics using a three-dimensional cellular automaton. J. Theor. Biol. 203 (4), 367–382. https://doi.org/10.1006/jtbi.2000.2000.

Kirschner, D.A., Hollingshead, C.J., 1980. Processing for electron microscopy alters membrane structure and packing in myelin. J. Ultrastruct. Res. 73 (2), 211–232. https://doi.org/10.1016/S0022-5320(80)90125-2.

Kumar, R., Nguyen, H.D., Macey, P.M., Woo, M.A., Harper, R.M., 2012. Regional brain axial and radial diffusivity changes during development. J. Neurosci. Res. 90 (2), 346–355. https://doi.org/10.1002/jnr.v90.210.1002/jnr.22757.

Latini, F., Fahlström, M., Berntsson, S.G., Larsson, E.-M., Smits, A., Ryttlefors, M., 2019. A novel radiological classification system for cerebral gliomas: the Brain-Grid. PLoS ONE 14 (1), e0211243. https://doi.org/10.1371/journal.pone.0211243.

Latini, F., Fahlström, M., Hesselager, G., Zetterling, M., Ryttlefors, M., 2020a. Differences in the preferential location and invasiveness of diffuse low-grade gliomas and their impact on outcome. Cancer Med. 9 (15), 5446–5458. https://doi.org/10.1002/cam4.v9.1510.1002/cam4.3216.

Latini, F., Hjortberg, M., Aldskogius, H., Ryttlefors, M., 2015. The use of a cerebral perfusion and immersion–fixation process for subsequent white matter dissection. J. Neurosci. Methods 253, 161–169. https://doi.org/10.1016/j.jneumeth.2015.06.019.

Latini, F., Mårtensson, J., Larsson, E.-M., Fredrikson, M., Åhs, F., Hjortberg, M., Aldskogius, H., Ryttlefors, M., 2017. Segmentation of the inferior longitudinal fasciculus in the human brain: a white matter dissection and diffusion tensor tractography study. Brain Res. 1675, 102–115. https://doi.org/10.1016/j.brainres.2017.09.005.

Latini, F., Trevisi, G., Fahlström, M., Jemstedt, M., Alberius Munkhammar, Å., Zetterling, M., Hesselager, G., Ryttlefors, M., 2020b. New insights into the anatomy, connectivity and clinical implications of the middle longitudinal fasciculus. Front. Neuroanat. 14 https://doi.org/10.3389/fnana.2020.610324.

Lee, H.-H., Yaros, K., Veraart, J., Pathan, J.L., Liang, F.-X., Kim, S.G., Novikov, D.S., Fieremans, E., 2019. Along-axon diameter variation and axonal orientation dispersion revealed with 3D electron microscopy: implications for quantifying brain white matter microstructure with histology and diffusion MRI. Brain Struct. Funct. 224 (4), 1469–1488. https://doi.org/10.1007/s00429-019-01844-6.

Liewald, D., Miller, R., Logothetis, N., Wagner, H.-J., Schüz, A., 2014. Distribution of axon diameters in cortical white matter: an electron-microscopic study on three human brains and a macaque. Biol. Cybern. 108 (5), 541–557. https://doi.org/10.1007/s00422-014-0626-2.

Louis, D.N., Perry, A., Reifenberger, G., von Deimling, A., Figarella-Branger, D., Cavenee, W.K., Ohgaki, H., Wiestler, O.D., Kleihues, P., Ellison, D.W., 2016. The 2016 World Health Organization Classification of Tumors of the Central Nervous System: a summary. Acta Neuropathol. 131 (6), 803–820. https://doi.org/10.1007/s00401-016-1545-1.

Mandonnet, E., Capelle, L., Duffau, H., 2006. Extension of paralimbic low grade gliomas: toward an anatomical classification based on white matter invasion patterns. J. Neurooncol. 78 (2), 179–185. https://doi.org/10.1007/s11060-005-9084-y.

Marín, O., Rubenstein, J.L.R., 2003. Cell migration in the forebrain. Annu. Rev. Neurosci. 26, 441–483. https://doi.org/10.1146/annurev.neuro.26.041002.131058.

Mathiisen, T.M., Lehre, K.P., Danbolt, N.C., Ottersen, O.P., 2010. The perivascular astroglial sheath provides a complete covering of the brain microvessels: an electron microscopic 3D reconstruction. Glia 58 (9), 1094–1103. https://doi.org/10.1002/glia.v58:910.1002/glia.20990.

Meoded, A., Poretti, A., Mori, S., Zhang, J., 2017. Diffusion Tensor Imaging (DTI). In: Reference Module in Neuroscience and Biobehavioral Psychology. Elsevier. https://doi.org/10.1016/B978-0-12-809324-5.02472-X.

Mukherjee, P., Miller, J.H., Shimony, J.S., Philip, J.V., Nehra, D., Snyder, A.Z., Conturo, T.E., Neil, J.J., McKinstry, R.C., 2002. Diffusion-tensor MR imaging of gray and white matter development during normal human brain maturation. AJNR Am. J. Neuroradiol. 23, 1445–1456.

Natté, R., van Eijk, R., Eilers, P., Cleton-Jansen, A.-M., Oosting, J., Kouwenhove, M., Kros, J.M., van Duinen, S., 2005. Multiplex ligation-dependent probe amplification for the detection of 1p and 19q chromosomal loss in oligodendroglial tumors. Brain Pathol. 15, 192–197. https://doi.org/10.1111/j.1750-3639.2005.tb00520.x.

Olivier, C., Cobos, I., Villegas, E.M.P., Spassky, N., Zalc, B., Martinez, S., Thomas, J.L., 2001. Monofocal origin of telencephalic oligodendrocytes in the anterior entopeduncular area of the chick embryo. Development 128, 1757–1769.

Painter, K.J., Hillen, T., 2013. Mathematical modelling of glioma growth: The use of Diffusion Tensor Imaging (DTI) data to predict the anisotropic pathways of cancer invasion. J. Theor. Biol. 323, 25–39. https://doi.org/10.1016/j.jtbi.2013.01.014.

Parisot, S., Darlix, A., Baumann, C., Zouaoui, S., Yordanova, Y., Blonski, M., Rigau, V., Chemouny, S., Taillandier, L., Bauchet, L., Duffau, H., Paragios, N., 2016. A Probabilistic Atlas of Diffuse WHO Grade II Glioma Locations in the Brain. PLoS ONE 11 (1), e0144200. https://doi.org/10.1371/journal.pone.0144200.

Partadiredja, G., Miller, R., Oorschot, D.E., 2003. The number, size, and type of axons in rat subcortical white matter on left and right sides: a stereological, ultrastructural study. J. Neurocytol. 32 (9), 1165–1179. https://doi.org/10.1023/B:NEUR.0000021910.65920.41.

Popova, S.N., Bergqvist, M., Dimberg, A., Edqvist, P., Ekman, S., Hesselager, G., Ponten, F., Smits, A., Sooman, L., Alafuzoff, I., 2014. Subtyping of gliomas of various WHO grades by the application of immunohistochemistry. Histopathology 64, 365–379. https://doi.org/10.1111/his.12252.

Qiu, D., Tan, L.-H., Zhou, K.e., Khong, P.-L., 2008. Diffusion tensor imaging of normal white matter maturation from late childhood to young adulthood: voxel-wise evaluation of mean diffusivity, fractional anisotropy, radial and axial diffusivities, and correlation with reading development. Neuroimage 41 (2), 223–232. https://doi.org/10.1016/j.neuroimage.2008.02.023.

Sarubbo, S., De Benedictis, A., Merler, S., Mandonnet, E., Balbi, S., Granieri, E., Duffau, H., 2015. Towards a functional atlas of human white matter. Hum. Brain Mapp. 36 (8), 3117–3136. https://doi.org/10.1002/hbm.v36.810.1002/hbm.22832.

Skjulsvik, A.J., Bø, H.K., Jakola, A.S., Berntsen, E.M., Bø, L.E., Reinertsen, I., Myrmel, K. S., Sjåvik, K., Åberg, K., Berg, T., Dai, H.Y., Kloster, R., Torp, S.H., Solheim, O., 2020. Is the anatomical distribution of low-grade gliomas linked to regions of gliogenesis? J. Neurooncol. 147 (1), 147–157. https://doi.org/10.1007/s11060-020-03409-8.

Smits, A., Jakola, A.S., 2019. Clinical Presentation, Natural History, and Prognosis of Diffuse Low-Grade Gliomas. Neurosurg. Clin. N. Am. 30 (1), 35–42. https://doi.org/10.1016/j.nec.2018.08.002.

Smits, A., Zetterling, M., Lundin, M., Melin, B., Fahlström, M., Grabowska, A., Larsson, E.-M., Berntsson, S.G., 2015. Neurological Impairment Linked with Cortico-

Subcortical Infiltration of Diffuse Low-Grade Gliomas at Initial Diagnosis Supports Early Brain Plasticity. Front. Neurol. 6 https://doi.org/10.3389/fneur.2015.00137.

Sotiropoulos, S.N., Moeller, S., Jbabdi, S., Xu, J., Andersson, J.L., Auerbach, E.J., Yacoub, E., Feinberg, D., Setsompop, K., Wald, L.L., Behrens, T.E.J, Ugurbil, K., Lenglet, C., 2013. Effects of image reconstruction on fiber orientation mapping from multichannel diffusion MRI: Reducing the noise floor using SENSE. Magn. Reson. Med. 70 (6), 1682–1689. https://doi.org/10.1002/mrm.v70.610.1002/mrm.24623.

Stikov, N., Campbell, J.S.W., Stroh, T., Lavelée, M., Frey, S., Novek, J., Nuara, S., Ho, M.-K., Bedell, B.J., Dougherty, R.F., Leppert, I.R., Boudreau, M., Narayanan, S., Duval, T., Cohen-Adad, J., Picard, P.-A., Gasecka, A., Côté, D., Pike, G.B., 2015. In vivo histology of the myelin g-ratio with magnetic resonance imaging. NeuroImage 118, 397–405. https://doi.org/10.1016/j.neuroimage.2015.05.023.

Suzuki, Y., Matsuzawa, H., Kwee, I.L., Nakada, T., 2003. Absolute eigenvalue diffusion tensor analysis for human brain maturation. NMR Biomed. 16 (5), 257–260. https://doi.org/10.1002/(ISSN)1099-149210.1002/nbm.v16:510.1002/nbm.848.

Szalisznyo, K., Silverstein, D.N., Duffau, H., Smits, A., Chacron, M.J., 2013. Pathological Neural Attractor Dynamics in Slowly Growing Gliomas Supports an Optimal Time Frame for White Matter Plasticity. PLoS ONE 8 (7), e69798. https://doi.org/10.1371/journal.pone.0069798.

Tournier, J.-D., Mori, S., Leemans, A., 2011. Diffusion tensor imaging and beyond. Magn. Reson. Med. 65 (6), 1532–1556. https://doi.org/10.1002/mrm.22924.

Van Essen, D.C., Smith, S.M., Barch, D.M., Behrens, T.E.J., Yacoub, E., Ugurbil, K., 2013. The WU-Minn Human Connectome Project: an overview. Neuroimage 80, 62–79. https://doi.org/10.1016/j.neuroimage.2013.05.041.

Wheeler-Kingshott, C.A.M., Cercignani, M., 2009. About "axial" and "radial" diffusivities. Magn. Reson. Med. 61 (5), 1255–1260. https://doi.org/10.1002/mrm.v61:510.1002/mrm.21965.

Wheeler-Kingshott, C.A.M., Cercignani, M., n.d. About "axial" and "radial" diffusivities 6.

Winklewski, P.J., Sabisz, A., Naumczyk, P., Jodzio, K., Szurowska, E., Szarmach, A., 2018. Understanding the Physiopathology Behind Axial and Radial Diffusivity Changes—What Do We Know? Front. Neurol. 9 https://doi.org/10.3389/fneur.2018.00092.

Wolburg, H., Noell, S., Mack, A., Wolburg-Buchholz, K., Fallier-Becker, P., 2009. Brain endothelial cells and the glio-vascular complex. Cell Tissue Res. 335 (1), 75–96. https://doi.org/10.1007/s00441-008-0658-9.

Yeh, F.-C., Verstynen, T.D., Wang, Y., Fernández-Miranda, J.C., Tseng, W.-Y., 2013. Deterministic diffusion fiber tracking improved by quantitative anisotropy. PLoS ONE 8 (11), e80713. https://doi.org/10.1371/journal.pone.0080713.

Yeh, F.-C., Wedeen, V.J., Tseng, W.-Y.-I., 2010. Generalized q-sampling imaging. IEEE Trans. Med. Imaging 29, 1626–1635. https://doi.org/10.1109/TMI.2010.2045126.

Yeh, F.-C., Zaydan, I.M., Suski, V.R., Lacomis, D., Richardson, R.M., Maroon, J.C., Barrios-Martinez, J., 2019. Differential tractography as a track-based biomarker for neuronal injury. Neuroimage 202, 116131. https://doi.org/10.1016/j.neuroimage.2019.116131.

Zemmoura, I., Blanchard, E., Raynal, P.-I., Rousselot-Denis, C., Destrieux, C., Velut, S., 2016. How Klingler's dissection permits exploration of brain structural connectivity? An electron microscopy study of human white matter. Brain Struct. Funct. 221 (5), 2477–2486. https://doi.org/10.1007/s00429-015-1050-7.

Zetterling, M., Berhane, L., Alafuzoff, I., Jakola, A.S., Smits, A., 2017. Prognostic markers for survival in patients with oligodendroglial tumors; a single-institution review of 214 cases. PLoS ONE 12 (11), e0188419. https://doi.org/10.1371/journal.pone.0188419.

Zetterling, M., Roodakker, K.R., Berntsson, S.G., Edqvist, P.-H., Latini, F., Landtblom, A.-M., Pontén, F., Alafuzoff, I., Larsson, E.-M., Smits, A., 2016. Extension of diffuse low-grade gliomas beyond radiological borders as shown by the coregistration of histopathological and magnetic resonance imaging data. J. Neurosurg. 125 (5), 1155–1166. https://doi.org/10.3171/2015.10.JNS15583.

Zhan, J.S., Gao, K., Chai, R.C., Jia, X.H., Luo, D.P., Ge, G., Jiang, Y.W., Fung, Y.-W., Li, L., Yu, A.C.H., 2017. Astrocytes in migration. Neurochem. Res. 42 (1), 272–282. https://doi.org/10.1007/s11064-016-2089-4.